Ocean Sci. Discuss., 10, 1997–2051, 2013
www.ocean-sci-discuss.net/10/1997/2013/
doi:10.5194/osd-10-1997-2013

Ocean Science
Discussions
Open Access

Adapting to life: ocean biogeochemical modelling and adaptive remeshing

J. Hill[1], E. E. Popova[2], D. A. Ham[3,4], M. D. Piggott[1,5], and M. Srokosz[2]

[1]Applied Modelling and Computation Group, Department of Earth Science and Engineering, Imperial College London, London, SW7 2AZ, UK
[2]National Oceanography Centre, Southampton, University of Southampton Waterfront Campus, European Way, Southampton, SO14 3ZH, UK
[3]Department of Mathematics, Imperial College London, London, SW7 2AZ, UK
[4]Department of Computing, Imperial College London, London, SW7 2AZ, UK
[5]Grantham Institute for Climate Change, Imperial College London, London, SW7 2AZ, UK

Received: 23 September 2013 – Accepted: 10 October 2013 – Published: 5 November 2013

Correspondence to: J. Hill (jon.hill@imperial.ac.uk)

Published by Copernicus Publications on behalf of the European Geosciences Union.

Abstract

An outstanding problem in biogeochemical modelling of the ocean is that many of the key processes occur intermittently at small scales, such as the sub-mesoscale, that are not well represented in global ocean models. As an example, state-of-the-art models give values of primary production approximately two orders of magnitude lower than those observed in the ocean's oligotrophic gyres, which cover a third of the Earth's surface. This is partly due to their failure to resolve sub-mesoscale phenomena, which play a significant role in nutrient supply. Simply increasing the resolution of the models may be an inefficient computational solution to this problem. An approach based on recent advances in adaptive mesh computational techniques may offer an alternative. Here the first steps in such an approach are described, using the example of a simple vertical column (quasi 1-D) ocean biogeochemical model.

We present a novel method of simulating ocean biogeochemical behaviour on a vertically adaptive computational mesh, where the mesh changes in response to the biogeochemical and physical state of the system throughout the simulation. We show that the model reproduces the general physical and biological behaviour at three ocean stations (India, Papa and Bermuda) as compared to a high-resolution fixed mesh simulation and to observations. The simulations capture both the seasonal and inter-annual variations. The use of an adaptive mesh does not increase the computational error, but reduces the number of mesh elements by a factor of 2–3, so reducing computational overhead. We then show the potential of this method in two case studies where we change the metric used to determine the varying mesh sizes in order to capture the dynamics of chlorophyll at Bermuda and sinking detritus at Papa. We therefore demonstrate adaptive meshes may provide a suitable numerical technique for simulating seasonal or transient biogeochemical behaviour at high spatial resolution whilst minimising computational cost.

OSD
10, 1997–2051, 2013

1 Introduction

Biogeochemical processes in the ocean are a key component of Earth's climate system and, in particular, of the carbon cycle. Understanding of the latter is crucial for projections of future climate change. However, modelling the biogeochemistry of the oceans presents a formidable challenge as many of the key processes occur at scales (both horizontal and vertical) not resolved by state-of-the-art climate models. Both mesoscale and sub-mesoscale processes are thought to be important; for example, in the supply of nutrients to the surface water of the oligotrophic gyres that cover one third of the Earth's surface (Oschlies, 2002; McGillicuddy et al., 2003; Lévy et al., 2012).

Therefore, in ocean biogeochemical models high horizontal resolution is important in order to capture the effects of mesoscale and sub-mesoscale fronts and eddies. Furthermore, many of the processes affecting biogeochemistry at the mesoscale and sub-mesoscale have significant vertical structure (Lévy et al., 2012). Thus there is also the need to have high vertical resolution to correctly represent vertical advection together with mixed layer deepening and shallowing. One way to address these needs is to increase the horizontal and vertical resolution of models, but this is computationally expensive. An alternative approach, pursued here, is to use mesh adaptivity in order to increase resolution only when and where it is required, thus reducing computational cost. Here, as a first step, the effectiveness of mesh adaptivity for providing appropriate vertical resolution is tested using a simple vertical column coupled physics and ecosystem model.

The behaviour of ocean ecosystems, and the associated biogeochemistry, is driven largely by physical processes (stirring and mixing). These vary depending on location; for example, differing between the subpolar and subtropical gyres. Therefore, simulations at different locations in the ocean may require different resolution structure (meshes) in the vertical. Adaptivity should allow the best mesh structure to be chosen for each location. By carefully selecting the adaptivity metric and parameters controlling the mesh, computational cost can in principle be minimised by reducing the number of

OSD
10, 1997–2051, 2013

degrees of freedom (Hiester et al., 2011; Hill et al., 2012). There is also a need to conserve biogeochemical quantities, so interpolation between meshes during adaptation can therefore be key in ensuring conservation.

In order to examine a range of conditions, three ocean stations (Fig. 1) were chosen to test the performance of mesh adaptivity in conjunction with ocean biogeochemistry models. These were Ocean Weather Station Papa, Ocean Weather Station India and the Bermuda Atlantic Time Series (BATS). These stations show very different mixed layer and biological behaviours and so test a model's ability to accurately simulate a range of physical and biological behaviours. Whilst Papa is ideal for carrying out one-dimensional studies due to the lack of significant horizontal advection (Denman and Miyake, 1973; Gaspar et al., 1990; Burchard and Bolding, 2001), India and Bermuda both experience significant horizontal advection. Previous attempts to model Bermuda in one dimension have resorted to ad hoc "fixes" (Anderson and Pondaven, 2003; Weber et al., 2007) in order to simulate the physical and biological behaviour here. However, the aims of these previous studies were to understand the processes occurring in more detail. In this study we are concerned with how well adaptive remeshing can replicate the results of a fixed mesh simulation whilst minimising the computational cost. We therefore do not expect a perfect match to observed data for these two stations, but the simulations must replicate the general observed behaviour at all three stations.

In Sect. 2 the numerical model used in this study is described, including the biogeochemical model used, turbulence parameterisation and mesh adaptivity algorithm. This model is then verified in Sect. 3, before the results from fixed mesh simulations are described. Section 4 then presents results from the adaptive mesh simulation. Finally, two experiments are described where the mesh is adapted to concentrate resolution not only in critical regions, but also to track sinking detritus at Station Papa and the sub-surface chlorophyll maximum at Bermuda. The paper then assesses the merits of the adaptive algorithm presented and draws some conclusions.

OSD
10, 1997–2051, 2013

2 Hydrodynamics model

Here, the non-hydrostatic Boussinesq equation system is considered in the context of Fluidity (Ford et al., 2004; Pain et al., 2005; Piggott et al., 2008), a highly flexible finite element/control volume modelling framework which allows for the numerical solution of the following set of equations:

$$\frac{\partial \boldsymbol{u}}{\partial t} + \boldsymbol{u}\cdot\nabla\boldsymbol{u} + f\boldsymbol{k}\times\boldsymbol{u} = -\nabla\left(\frac{p}{\rho_0}\right) - \frac{\rho}{\rho_0}g\boldsymbol{k} + \nabla\cdot(\boldsymbol{\nu}\nabla\boldsymbol{u}), \tag{1}$$

$$\nabla\cdot\boldsymbol{u} = 0, \tag{2}$$

$$\frac{\partial T}{\partial t} + \boldsymbol{u}\cdot\nabla T = \nabla\cdot(\boldsymbol{\kappa}_\mathrm{T}\nabla T), \tag{3}$$

$$\frac{\partial S}{\partial t} + \boldsymbol{u}\cdot\nabla S = \nabla\cdot(\boldsymbol{\kappa}_\mathrm{S}\nabla S), \tag{4}$$

$$\rho \equiv \rho(T,S), \tag{5}$$

where $\boldsymbol{u}$ is the 3-D velocity vector, t represents time, p is the pressure, g is the acceleration due to gravity acting in the $\boldsymbol{k} = (0,0,1)^\mathrm{T}$ direction, T is temperature and S is salinity. ρ is the density which is given in terms of an equation of state function with temperature and salinity as input arguments, and ρ_0 is a constant background value for density. $\boldsymbol{\nu}$ is the tensor of kinematic viscosities and $\boldsymbol{\kappa}_\mathrm{T}$, $\boldsymbol{\kappa}_\mathrm{S}$ are the thermal and saline diffusivity tensors respectively. f is the Coriolis parameter which in this work is assumed constant. We also assume, for simplicity, a Cartesian coordinate system with $\boldsymbol{k}$ pointing in the direction of gravity.

The above equations were discretised on an unstructured mesh of tetrahedral elements using the finite element method. The form of the discretisation is determined by the order of the polynomials used for the different solution variables and whether or not they are continuous or discontinuous across element faces.

OSD
10, 1997–2051, 2013

Here, we use linear continuous Galerkin method for velocity and pressure, with a control volume formulation used for all tracer fields, including turbulence and biological tracers. For further details refer to Piggott et al. (2008, 2009).

2.1 Boundary conditions

The domain used is pseudo-1-D, 100 m square in the horizontal with depths of either 1000 m for Station Papa and Bermuda, or 2000 m for Station India. This ensures the maximum mixed layer depth is well above the lower boundary at all stations. The lateral boundaries have a Dirichlet condition applied to the velocity such that the vertical component is zero. The top and bottom surfaces also have this condition applied. Boundary conditions for the turbulent quantities are as described in (Hill et al., 2012) and are Neumann conditions for both turbulent equations. The upper surface is subjected to heat, momentum and salinity fluxes. These are derived via the Large and Yeager (2004) bulk formulae, with atmospheric data supplied from ERA40 (Uppala et al., 2005). Both Station Papa and Station India use atmospheric forcing from 1970 onwards as this is when most observation data from those stations is available. Bermuda uses atmospheric forcing from 1980 onwards; again as most observational data was available during this period. Briefly, the three surface kinematic fluxes calculated: heat – $\langle w\theta \rangle$, salt – $\langle ws \rangle$, and momentum – $\langle wu \rangle$ and $\langle wv \rangle$, can be related to the surface fluxes of heat Q, the freshwater F, and the momentum $\boldsymbol{\tau} = (\tau_u, \tau_v)$, via:

$$\langle w\theta \rangle = Q\left(\rho c_p\right)^{-1} \tag{6}$$

$$\langle ws \rangle = F\left(\rho^{-1} S_0\right) \tag{7}$$

$$\left(\langle wu \rangle, \langle wv \rangle\right) = \boldsymbol{\tau}\rho^{-1} = (\tau_u, \tau_v)\rho^{-1}, \tag{8}$$

where ρ is the ocean density, c_p is the heat capacity ($4000\,\mathrm{J\,kg^{-1}\,K^{-1}}$) and S_0 is a reference ocean salinity, which is the current sea surface salinity. These fluxes are then applied as upper-surface Neumann boundary conditions on the appropriate fields.

OSD
10, 1997–2051, 2013

2.2 Biology model

The biology model in Fluidity contains a number of different sub-models. All are population level models where variables evolve under an advection-diffusion equation similar to that for other tracers, such as temperature and salinity, but modified by the addition of a source term which contains the interactions between the biological fields. In this case a six-component model similar to the globally applicable model of Popova et al. (2006) was used.

Heuristically, the model consists of nutrients (ammonium and nitrate) which are fixed by phytoplankton in the presence of sunlight. Zooplankton grazes on phytoplankton and detritus partially recycling them back into inorganic nutrients and partially converting into detritus. Phytoplankton and zooplankton mortality are also producing detritus which is gradually converted to back nutrients as it sinks through the water column. In addition, chlorophyll is calculated as an independent state variable and presented here to allow comparisons to data.

For more details of this model, see Appendix A1.

2.3 Vertical turbulence model

The generic length scale (GLS) turbulence parameterisation is capable of modelling vertical turbulence at a scale finer than that of the mesh. As the GLS model is a RANS parameterisation there is no dependency on the mesh resolution, provided the advective model simulates no turbulent processes, so is ideal for adaptive ocean-scale problems. GLS has the additional advantage that it can be set-up to behave as a number of classical turbulence models: $k-\epsilon$, $k-kl$, $k-\omega$, and an additional model based on Umlauf and Burchard (2003), the *gen* model. The GLS model has been implemented within Fluidity and shown to work well with adaptive remeshing (Hill et al., 2012).

All implementations rely on a local, temporally varying, kinematic eddy viscosity ν_M that parametrises turbulence (local Reynolds stresses) in terms of mean-flow quantities (vertical shear). In addition, a buoyancy term that parametrises the kinematic eddy

OSD
10, 1997–2051, 2013

diffusivity, ν_H is also implemented:

$$\overline{u'w'} = -\nu_M \frac{\partial u}{\partial z}, \quad \overline{v'w'} = -\nu_M \frac{\partial v}{\partial z}, \quad \overline{w'\rho'} = -\nu_H \frac{\partial \rho}{\partial z}, \tag{9}$$

with

$$\nu_M = \sqrt{k} l S_M + \nu_M^0, \quad \nu_H = \sqrt{k} l S_H + \nu_H^0. \tag{10}$$

Here we follow the notation of Umlauf and Burchard (2003), where u and v are the horizontal components of the Reynolds-averaged velocity along the x- and y-axes, w is the vertical velocity along the vertical z-axis, positive upwards, and u', v' and w' are the components of the turbulent fluctuations about the mean velocity. ν_H^0 is the background diffusivity, ν_M^0 is the background viscosity, S_M and S_H are often referred to as stability functions, k is the turbulent kinetic energy, and l is a length-scale. When using GLS the values of ν_M and ν_H become the vertical components of the tensors $\boldsymbol{\nu}$ and $\boldsymbol{\kappa}_\mathrm{T}$ in Eqs. (1) and (3) respectively. Other tracer fields, such as salinity use the same diffusivity as temperature, i.e. $\boldsymbol{\kappa}_\mathrm{T} = \boldsymbol{\kappa}_\mathrm{S}$.

The generic length scale turbulence closure model (Umlauf and Burchard, 2003) is based on two equations, for the transport of turbulent kinetic energy (TKE) and a generic second quantity, Ψ. The TKE equation is:

$$\frac{\partial k}{\partial t} + \boldsymbol{u}_i \frac{\partial k}{\partial x_i} = \frac{\partial}{\partial z}\left(\frac{\nu_M}{\sigma_k}\frac{\partial k}{\partial z}\right) + P + B - \epsilon, \tag{11}$$

where σ_k is the turbulence Schmidt number for k, and P and B represent production by shear and buoyancy which are defined as:

$$\begin{aligned} P &= -\overline{u'w'}\frac{\partial u}{\partial z} - \overline{v'w'}\frac{\partial v}{\partial z} = \nu_M M^2 \\ M^2 &= \left(\frac{\partial u}{\partial z}\right)^2 + \left(\frac{\partial v}{\partial z}\right)^2, \end{aligned} \tag{12}$$

OSD
10, 1997–2051, 2013

$$B = -\frac{g}{\rho_0}\overline{\rho' w'} = -\nu_H N^2$$
$$N^2 = -\frac{g}{\rho_0}\frac{\partial \rho}{\partial z} \quad (13)$$

Here N is the buoyancy frequency. The dissipation is modelled using a rate of dissipation term:

$$\epsilon = \left(c_\mu^0\right)^{3+\frac{p}{n}} k^{\frac{3}{2}+\frac{m}{n}} \Psi^{-\frac{1}{n}}, \quad (14)$$

where c_μ^0 is a model constant used to make Ψ identifiable with any of the other two-equation models, e.g. kl, ϵ, and ω.

There is also the option to add an extra term to account for additional oceanic physics, such an internal waves breaking. This is based on the NEMO ocean model (Madec, 2008) and takes a user-defined percentage of the surface k and adds it down-depth using an exponential profile:

$$k(z) = k_0(z) + \alpha k_{\text{sur}} \exp\left(-z/l_k\right) \quad (15)$$

where k is the new turbulent kinetic energy value at depth, z, k_0 is the original turbulent kinetic energy, k_{sur} is the surface turbulent kinetic energy, α is a constant for the amount (percentage) of surface turbulent kinetic energy to transfer down the column, and l_k is a length scale (m) over which this decy occurs. In this work, $\alpha = 0.05$ and $l_k = 30$.

The second equation is:

$$\frac{\partial \Psi}{\partial t} + \boldsymbol{u}_i \frac{\partial \Psi}{\partial x_i} = \frac{\partial}{\partial z}\left(\frac{\nu_M}{\sigma_\Psi}\frac{\partial \Psi}{\partial z}\right) + \frac{\Psi}{k}(c_1 P + c_3 B - c_2 \epsilon F_{\text{wall}}), \quad (16)$$

The parameter σ_Ψ is the Schmidt number for Ψ and c_i are constants based on experimental data. The value of c_3 depends on whether the flow is stably stratified (in which

OSD
10, 1997–2051, 2013

case $c_3 = c_3^-$) or unstable ($c_3 = c_3^+$). Here,

$$\Psi = \left(c_\mu^0\right)^p k^m l^n, \tag{17}$$

and

$$l = \left(c_\mu^0\right)^3 k^{\frac{3}{2}} \epsilon^{-1}. \tag{18}$$

For this study we used GLS with parameters set to transform the equations into the classic $k - \epsilon$ model. See Hill et al. (2012) for details.

2.4 Dynamic adaptive mesh optimisation

The discussion here largely follows that of Hill et al. (2012), which can be consulted for more details. The mesh adaptivity algorithm used in this work attempts to optimise the size as well as the shape of individual elements of the mesh in order to minimise an optimisation functional (Pain et al., 2001; Piggott et al., 2005, 2008). In Fluidity, mesh adaptivity aims to increase resolution in regions of the domain with large curvatures of given fields and decrease resolution elsewhere. This approach allows good representation of the small-scale dynamics and sharp gradients without the need for high spatial resolution throughout the entire domain, (Piggott et al., 2005). The mesh is adapted through a series of local topological and geometrical operations as described in (Pain et al., 2001). In this work we adapt in the vertical direction only. A single column of mesh vertices is first adapted. This column is then replicated to the other three columns, which are then joined to form a pseudo-1-D column of tetrahedra. The location of the vertices is constructed such that all elements in that first one dimensional column have unit edge-length when measured with respect to a given metric, M.

In Fluidity a relatively simple metric is employed. For chosen fields, f_i, metrics, M_i are defined by:

$$M_i = \det|H_i|^{-\frac{1}{2p+n}} \frac{|\mathbf{H}_i|}{\varepsilon_i}, \tag{19}$$

OSD
10, 1997–2051, 2013

where ε_i is a user-defined weight corresponding to the field under consideration and $|\mathbf{H}_i|$ is the Hessian matrix for that field where the absolute values of its eigenvectors have been taken, $p \in \mathbb{Z}$ and n is the dimension of the space (Loseille and Alauzet, 2011). The final metric used, M, is formed from a superposition of the metrics for individual fields: $M = \bigcup_i M_i$, (Pain et al., 2001). In the work presented here we test values of p of 2 and ∞ as both have been used in previous work, but $p = 2$ has shown superior results in resolving both weak and strong curvatures simultaneously within the same simulation (Loseille and Alauzet, 2011; Hiester et al., 2011). The use of a tensor for the metric allows anisotropic directional information to be included and influence the adaptivity. ε may vary spatially and temporally, but neither is utilised here. In general, for a given solution field, decreasing ε will lead to greater refinement of the mesh and increasing ε will lead to more coarsening. The maximum and minimum edge-length allowed can also be specified. For more details see Pain et al. (2001); Piggott et al. (2005, 2008); Hiester et al. (2011) and references therein.

The mesh is adapted at run-time and the frequency with which it adapts can also be specified. After an adapt the solution fields must be interpolated from the pre- to post-adapt meshes. Two methods are available "consistent-interpolation" and "bounded Galerkin-projection" (Farrell et al., 2009). All prognostic fields are interpolated, along with any diagnostic fields as required.

The adaptive mesh technique used in Fluidity differs from previous implementations of adaptive mesh techniques used in similar models in that the number of elements (or in the case of finite-difference models, grid points) can change throughout the simulation. For example, in both Burchard and Beckers (2004) and Hanert et al. (2006) the number of grid points remains fixed: the adaptive mesh simply moves them to locations to minimise the error metric; in essence a mesh movement algorithm. The techniques of Burchard and Beckers (2004) have been extended to 3-D by allowing each horizontal location to have a different vertical mesh (Hofmeister et al., 2010). Again, the number of grid points is fixed. Adaptive techniques have been shown to reduce levels of numerical mixing in a number of idealised examples (Hofmeister et al., 2010). It is important

OSD
10, 1997–2051, 2013

to note here, that Fluidity allows a great deal of flexibility in choosing the metric, unlike in the previous studies described above. Here we investigate how the choice of which fields (physical and biological) are included in the metric affects a simulation. We do not investigate the effects of changing the user-defined weights ε; they are chosen to give a reasonable result and may not be optimal. For the purposes of this paper ε being sub-optimal is not critical.

3 Model verification

For all stations we have run the simulations on a number of fixed meshes, varying the vertical resolution between 20 m and 2.5 m. The fixed mesh simulation will be used as verification of correct function and having established that, we will use the highest resolution (2.5 m) fixed mesh simulation as "truth" when assessing the performance of the adaptive mesh simulations. In addition we will use qualitative comparisons to observational data at each station to ensure the model performs as expected, given the lack of horizontal dynamics.

A standard Root Mean Square error (RMS) was used to assess model performance. The RMS error, ϵ is calculated as:

$$\epsilon = \sqrt{\frac{\sum_{i=1}^{n} (x_i - y_i)^2}{n}}, \tag{20}$$

where x_i is the quantity being assessed in the high resolution simulation, y_i is the value of the quantity produced by the simulation being considered. All simulations were run for three years. Output for all runs was produced every 12 h, giving $n = 2190$. For each field of interest a separate ϵ is calculated, giving ϵ_{MLD} for the mixed layer depth. For biological quantities the $\mathrm{L2}_{\mathrm{norm}}$ of the water column was used, giving, ϵ_{N} for nutrients, ϵ_{P} for primary productivity, ϵ_{C} for chlorophyll, and ϵ_{Z} for zooplankton. We first examine

OSD
10, 1997–2051, 2013

a single fixed mesh case for each station, comparing them to available observational data from Kleypas and Doney (2001) and Popova et al. (2006), before showing that the simulated response depends on the model's vertical resolution.

Station Papa in the north-west Pacific is an ideal testing station for a one-dimensional simulation. There is little horizontal advection, and as such, Papa has been used to assess numerical models (Denman and Miyake, 1973; Burchard and Bolding, 2001; Hill et al., 2012). Fluidity has also been previously shown to work well at replicating the expected physics with adaptive meshes ere (Hill et al., 2012). Papa's distinguishing feature is that nutrients are not limited and hence surface nutrients exhibit only a small seasonal variation. The results of the biogeochemical model show good agreement with measured data (Fig. 2), replicating the major features of this station. The surface nutrients show the desired dip over the summer months, though this is not quite as pronounced as the observed data. However, the surface chlorophyll shows excellent agreement to observed data, as does the integrated primary production (note: this is integrated over the mixed layer).

The model result at Bermuda, unlike Papa, shows some differences to the measured data (Fig. 3). The surface nutrient shows the nutrient-limited behaviour, but the limited nutrients occur too early in the season. The third winter (days 700–900) shows a marked deepening of the mixed layer. This is due to extreme surface forcing behaviour. Longer simulations (not shown) show a return to the more normal behaviour seen in years one and two. Surface chlorophyll values lie on the upper limit of observed data, with a small peak in the spring. However, the primary productivity (N.B. averaged over mixed layer depth) is around a factor of two too low. However, given we are simulating an isolated one-dimensional column, without any horizontal transport of quantities in or out of the domain, we believe this is a reasonable result. There is a substantial subsurface chlorophyll maxima (Fig. 4) as has been shown in measured observation and is a similar magnitude to that obtained in previous modelling studies (e.g. Anderson and Pondaven, 2003).

OSD
10, 1997–2051, 2013

Unlike the previous stations there is a lack of MLD data for Station India. However, the model, again, gives a reasonable result (Fig. 5). The spring bloom (as shown by the surface chlorophyll) happens around 30 days early, with a peak that is perhaps a factor of four too high. Similarly, the integrated primary productivity (N.B. integrated over the mixed layer) shows a peak of around 2–3 times the observed value at the same time. However, the values during the rest of the year lie around the lower limit of observed data. Surface nutrients show good agreement with the timing of the spring decrease, but is perhaps a factor of two too high during the summer months.

3.1 Resolution dependence

For all stations the simulation was re-run with different resolution meshes, all with uniform vertical resolution, ranging from 2.5 to 20 m. There were no other changes made to the simulation set-up. The highest resolution (2.5 m) is then used as "truth" in the comparisons. Figures 6 to 8 show a single year (year two of the three year simulation to allow for model spin-up) for each station. For Station Papa (Fig. 6) there is a noticeable difference in mixed layer depth behaviour with higher resolutions showing deeper winter mixing. This in turn affects the upwelling of nutrients, which show a marked jump when resolution is refined from 10 to 5 m. Both 5 and 2.5 m show broadly similar patterns. The difference in upwelling nutrients then affects the primary productivity, and surface chlorophyll shows a difference in peak surface chlorophyll of around 20 days. Bermuda shows a similar pattern (Fig. 7) with increased resolution producing higher peak nutrients due to increased upwelling, which in turn leads to increased surface chlorophyll. Finally, Station India (Fig. 8) shows a marked increase in primary productivity within the MLD, which is doubled when resolution is refined from 20 to 2.5 m. The surface nutrient data shows little difference with resolution, so a sensible interpretation is that this is due to the slight increase in summer MLD depths with increased resolution. It is therefore clear that all stations show a response to vertical resolution which is the result of a complex interaction between the mixing caused by the vertical turbulence model and the biological sources and sinks.

OSD
10, 1997–2051, 2013

Resolution dependence can also be seen in vertical profiles. chlorophyll vertical profiles were taken at day 547 (mid-summer of the second year) and day 730 (mid-winter at the end of the second year) (Fig. 9). Each station shows a change in the simulated value with increasing resolution. This is perhaps most pronounced at Station Papa during the winter, where the mixed layer depth increases from around 100 to nearly 120 m when resolution is increased from 20 to 2.5 m. Bermuda shows a decrease of both winter and summer sub-surface chlorophyll maxima with increasing resolution. These vertical profiles show that the model is stable; producing adequate results at even low resolution; and that vertical resolution does affect the profile simulated.

The response to resolution can be examined more quantitatively using a simple convergence test. Although convergence is non-trivial for non-linear dynamics (Hill et al., 2012), a decrease in error should be seen with increasing vertical resolution. For all stations there is clear convergence (a decrease in error) for the mixed layer depth (Tables 2–4). Ideally, for the set-up described previously, this should be at least first-order convergence. Both Bermuda and Station Papa show this behaviour but Station India does not (though there is still a decrease in error with increasing resolution). However, for most variables there is a decrease in the error measure at each station. The surface nutrients error stays approximately constant at both Bermuda and Station India (Tables 3 and 4). Despite these exceptions there is a clear dependence on resolution, with higher resolutions generally matching the highest resolution simulation with higher accuracy. At Papa, all biological quantities bar nutrients show a general convergence in error as resolution is increased (Table 2). The error at 10 m vertical resolution appears to be double that expected, but there is a convergence in error from 10 to 5 m. Bermuda shows clear first order convergence of mixed layer depths and zooplankton; and less certain convergence of chlorophyll (Table 3). Surface nutrient error appears to be constant, as does primary productivity (average over the mixed layer depth). Finally, Station India shows a general convergence with increasing resolution for all biological quantities, though not at first order (Table 4).

OSD
10, 1997–2051, 2013

From these results we can see that there is a general decrease in error to the highest resolution run with increasing resolution. Therefore, using vertical adaptivity should allow a minimisation in the number of elements within the computational mesh whilst ensuring error does not increase to an unreasonable level.

4 Adaptivity

We have carried out the same simulations as above using an adaptive mesh guided by a variety of different metrics and, in addition, we have tested different interpolation methods at Station Papa. For simplicity simulations at the three test station used the same adaptivity settings. Adaptivity was performed every five hours. This allows changes in ocean surface forcing (which has a temporal frequency of six hours) to be captured, along with diurnal fluctuations. Over a three year simulation a total of 5256 adapts are thus performed. This is a large number and therefore any additional numerical diffusivity or noise derived from adapting the mesh will be evident in the final simulation results when compared to the fixed mesh simulations. The minimum and maximum edge lengths permitted are set to 5 m and 50 m, respectively. We therefore hope to find the adaptive simulations are equivalent to the 5 m fixed resolution simulations, but use substantially fewer elements; hence showing a reduced computational cost.

The adaptive algorithm was performed on a single vertical column of mesh vertices and the position of these were replicated to the other three columns. In this way we obtained a layered mesh, with vertical resolution of the layers varying according to the chosen metric and the simulated state at the time of the adapt. Apart from the adaptive mesh, the simulations were completely identical to the fixed mesh simulations.

OSD
10, 1997–2051, 2013

4.1 Metric formation

The metric used to adapt the mesh is crucial to obtaining an optimal simulation (Hiester et al., 2011). Here, we test four different metric formulations which govern vertex positions: *PAR*, *Bio*, *Bio and Phys*, and *Phys*. These use the photosynthetic active radiation only (PAR), biological fields only (Bio), physical fields only (Phys) or a combination (Bio and Phys). The same metrics are used for all three test stations as we are attempting to provide a metric formulation that works well in a variety of ocean settings and to avoid "tweaking" of the metric for a particular location. The physical fields used are the density and velocity, and the biological fields used are the nutrients and PAR. Details of the fields used and the weighting of each field are given in Table 1.

The aim of choosing these fields is to enable tracking of the mixed layer depth variation on both a daily and seasonal level. This will concentrate resolution only where changes of the above quantities are large, minimising computational cost elsewhere. The physical fields choosen are density and velocity. Density will show a steep vertical change at the base of the mixed layer, whilst velocity varies strongly in the top few metres of the water column. However, if winds strengthen more resolution will be added as the mixing deepens. The biology tracers chosen are the nutrients and PAR. Fluxes of nutrients from depth are the main cause of plankton blooms at both India and Bermuda. However, the nutrient high and hence phytoplankton high, may not be at the surface; this is the case in Bermuda where there is a significant sub-surface chlorophyll maximum. By tracking the nutrient fluxes closely we aim to also then track the other biological tracers as a consequence. In contrast Station Papa shows only weakly varying surface nutrient changes. However, the upward flux of nutrients can lead to erroneous timings of the spring bloom. Therefore, the base of the mixed layer depth shows a substantial vertical nutrient change and hence adding resolution here should minimise vertical numerical diffusivity. PAR is important only in the top 100 m of the domain and varies daily and hence adding this field to the metric will add extra resolution during daylight hours down to the bottom of the photic zone.

OSD
10, 1997–2051, 2013

The meshes produced by the adaptive algorithm showed broadly similar features between different metrics for each particular site (Fig. 10). Comparing those produced by the metric using both the biological and physical fields show the mesh tracking the behaviour of the mixed layer depth. In addition, high resolution is maintained in the photic layer, but reduces with the mixed layer when the mixed layer depth increases substantially.

4.2 Interpolation

Three different interpolation methods were tested in this work. Linear interpolation, which is bounded but non-conservative; Galerkin projection, which is conservative and can be made bounded at the expense of a minimal amount of diffusion (Farrell et al., 2009); and a mixture of the two, where Galerkin projection was used for biological tracers, and consistent interpolation was used for physical quantities. It is anticipated that conservation of the integral of biological quantities is crucial to obtaining a satisfactory solution, but that the physical quantities, velocity, temperature and salinity, only require consistent interpolation (Hill et al., 2012). As consistent interpolation is less computationally demanding than Galerkin projection, further savings in computational cost over and above that of adaptivity can be gained using consistent interpolation where it is adequate.

The tests at Station Papa (Fig. 11) show that Galerkin projection for all fields gives the best result for both physical behaviour (MLD) and biological quantities. In particular, there is a significant surface nutrient drift when using consistent interpolation, and less so when using a mixed formulation. Using Galerkin projection on both physical and biological fields gives a result that is almost identical to the fixed mesh simulation. The MLD behaviour changes in response to the interpolation method used, with a marked shoaling of the mixed layer depth around day 800 when using consistent or mixed interpolation. The mixed interpolation formulation performed only slightly better in this regard and using Galerkin projection on the turbulent parameterisation quantities only improved the solution slightly (results not shown). These result contrast to those

OSD
10, 1997–2051, 2013

presented in Hill et al. (2012), where consistent interpolation was used and adaptivity performed well at Station Papa. However, here we have added the additional term to simulate internal wave breaking (Eq. 15) and the metric tuned to Station Papa only, with a lower minimum edge length. It is also worth noting that the temperature and salinity fields showed little or no difference between the fixed and adaptive simulations; it is the biological tracers that highlight undesired behaviour of the adaptive runs. Galerkin projection is therefore used for all subsequent adaptive simulations.

4.3 Station Papa

All adaptive simulations at Station Papa completed successfully and produced results that are a reasonable fit to measured data (Fig. 12). Using a metric formed of physical or physical and biological quantities produces results that are not significantly different from that of the uniform 5 m resolution simulation (Table 5). All tracers give similar or better results than the 5 m fixed simulation, though given the lack of convergence shown in some of these quantities some caution must be used in interpreting these values. It is clear that using only biology or just PAR to form the metric is not adequate at this location as the values of the RMS errors, ϵ, for all tracers are substantially larger, apart from primary productivity, which has already been identified as potentially problematic in using as an assessment of performance.

4.4 Bermuda

Not all adaptive simulations were effective at Bermuda. Using either PAR or biology only to form the metric results in simulations failing with a solver error soon after the first or second adapt. This is attributed to insufficient mesh resolution to ensure stability for the GLS turbulence parameterisations. Unlike Station Papa, the mixed layer depth is well below the photic zone in the initial stages of the simulation. However, both simulations using either physics only or biology and physics performed well. Both gave similar results, quantitatively (Table 6) and qualitatively (Fig. 13). The two metrics also gave

OSD
10, 1997–2051, 2013

lower values of ϵ_C and ϵ_Z, but, as with Station Papa, these values should interpreted with some caution.

4.5 Station India

All adaptive simulations produced excellent results at Station India regardless of metric used. Minor differences in the timing of the spring bloom occurred with the biology only metric occurring some 25 days later than the fixed mesh simulation. The biology only metric also showed an increase in the number of shoaling excursions in the spring. These did not occur when using other metrics or in the fixed mesh simulations. There are also minor differences in the magnitude of the integrated primary productivity, but these variations are much lower than those observed when changing resolution in the fixed mesh simulations (Fig. 8).

4.6 Summary of adaptive results

Adaptivity can clearly be used simulate the three ocean stations successfully using a variety of mesh metrics. Some metric/station combinations perform better than others, as would be expected. As well as reproducing the surface values and the mixed layer depth the adaptive simulations also reproduce the vertical profiles of biological parameters (see Fig. 15 for chlorophyll and compare to Fig. 9).

The effect of adaptivity is clearly seen in the meshes produced by the simulations (Fig. 10). All stations show much higher resolution around the mixed layer depth, as expected, with decreased resolution when the mixed layer depth is deep (for example at Station India). The meshes contains far fewer elements than the high resolution fixed mesh simulations and are therefore more computationally efficient.

For all stations it is important to include velocity and density in the metric (labelled as "physics" in all figures) and the inclusion of nutrients appears to be only of minor importance. However, using nutrients only or PAR can lead to an unstable simulations and moreover, when the simulation is stable, gives much larger errors than the metrics that

OSD
10, 1997–2051, 2013

include the physics. The simulated physics drives the biology and it is therefore crucial to include measures of the physical system in the metric to correctly simulate the physical behaviour of the system. Physical measures used here are the vertical changes in velocity and density. However, turbulent kinetic energy, temperature or salinity may also be sensible choices (Hill et al., 2012). Accounting for physical behaviour in the metric appears to be sufficient for a successful simulation of biological behaviour. However, if the physical properties are well simulated then the biological process do not necessarily also need including in the metric also for reasonable output.

5 Specific adaptive examples

One of the primary advantages of the approach outlined above is that the metric used to calculate the mesh edge length can be composed of any simulated or diagnosed fields. We show the potential of that method here by simulating Bermuda with a metric focusing on chlorophyll, and Station Papa concentrating on sinking detritus. These simulations show how the mesh is able to adapt to the particulars of the simulation, tracking transient behaviour but with a lower computational overhead than a high-resolution fixed mesh simulation.

The first experiment attempts to track falling detritus in the Station Papa case. The detritus field is added to the adaptivity metric. The result, compared to the previous adaptive simulation using only nutrients, velocity and density in the metric, shows a considerable change in the detritus concentration at depth (Fig. 16). In the original adaptive simulation, the detritus field is smoothed out at depths of over 300 m as the resolution here is relatively coarse. The effect of adding detritus to the mesh metric is as expected, the field maintains the sharp boundaries as it sinks, replicating the highest resolution fixed mesh simulation. This is clearly seen in the resulting computational mesh (Fig. 17).

A similar result is seen at Bermuda where chlorophyll is added to the mesh metric. Here, we see the subsurface chlorophyll maximum is maintained correctly (Fig. 18),

OSD
10, 1997–2051, 2013

where in the previous adaptive simulation the simulated value is lower around day 130 than the fixed mesh simulation. This is not the case when chlorophyll is added to the mesh metric. Similarly, the effect can be seen in the resulting mesh (Fig. 17).

For both simulations there is, of course, an increase in the number of elements used compared to the original adaptive simulations, but the average number of elements is still much lower than the high resolution fixed mesh simulation, and accordingly, the run times are much lower. The Bermuda simulation used an average of 437 elements (576 maximum, 301 minimum). Compared to a fixed mesh of uniform resolution 2.5 m (2400 elements) this a five-fold reduction in elements on average. Similarly, simulating detritus at Station Papa used an average of 726 elements (507 minimum, 1120 maximum), compared to 2400 elements used in the 2.5 m fixed mesh simulation – a three-fold reduction. Even given the time taken to adapt the mesh, the large reduction in the number of elements used gives a substantial computational saving. This saving will increase when moving to large-scale three-dimensional simulations.

6 Conclusions

We have shown that Fluidity can successfully replicated expected behaviour at three disparate biogeochemical stations. Both fixed and adaptive mesh simulations show very similar behaviour. Adaptivity requires a metric to be formed, which can be constructed from any number of simulated fields. Here, we have tested four different metrics, but only two are successful at all three stations; a mixture of using biological and physical tracers, and using physical tracers only. Using only biological tracers or PAR fails at Bermuda, although further tuning may allow successful simulation at this location. The reason for this result is that the simulated physics drives the biology and is therefore crucial to correctly simulate the biological behaviour of the system. In addition, if the physical properties are well simulated then the biological process do not necessarily need including in the metric also for reasonable output.

OSD
10, 1997–2051, 2013

It has been shown that a key component of successful adaptive simulation is to conservatively interpolate fields between the previous and new mesh following an adapt. Both consistent and the use of conservative interpolation for only a subset of solution fields is not sufficient. In addition, we also found that for this pseudo-1-D domain each column of the domain must be identical. Fully three-dimensional simulations where each column contains different number of nodes induced additional vertical diffusivity. More work is required to ascertain if this effect is present in simulations using larger horizontal resolution, as would be the case in global- or regional-scale ocean models.

Ocean biogeochemical numerical models may require high numerical resolution in order to simulate measured data accurately. Regardless of whether a high horizontal resolution is used or adaptive meshes are used, the vertical resolution does not need to be constant for each spatial location. Instead, as is shown here, the resolution only needs to be placed at key locations in the vertical. Enabling higher resolution around the mixed layer depth and within the upper layers of the ocean is sufficient for replicated high resolution fixed mesh simulations. However, additions to the metric of other fields allows for the tracking of transient features and of other fields, such as detritus or chlorophyll. This is a powerful tool in tracking features of interest whilst minimising computational overhead.

Adaptive remeshing shows good potential to reduce computational costs whilst maintaining, or even increasing, vertical resolution, but only where it is required.

Appendix A

Biology model

As stated in the main body of the text, the biogeochemistry model used in this paper was based on that of Popova et al. (2006). Note however that the equations here are continuous for all depths, which was not true in Popova et al. (2006) were different source terms where used below the photic zone. The model parameters have also

OSD
10, 1997–2051, 2013

been fitted to match the data at all three test sites. The six components of the model are: nutrients (ammonium and nitrate), phytoplankton, chlorophyll, zooplankton and detritus.

A1 Biological source terms

The source terms for phytoplankton (P), chlorophyll (Chl), zooplankton (Z), nitrate (N), ammonium (A), and detritus (D) respectively are given by the following expressions:

$$S_P = PJ(Q_N + Q_A) - G_P - De_P, \quad (A1)$$

$$S_{Chl} = (R_P J(Q_N + Q_A)P + (-G_P - De_P))(\theta/\zeta), \quad (A2)$$

$$S_Z = \delta(\beta_P G_P + \beta_D G_D) - De_Z, \quad (A3)$$

$$S_N = -JPQ_N + De_A, \quad (A4)$$

$$S_A = -JPQ_A + De_D + (1-\delta)(\beta_P G_P + \beta_D G_D) + (1-\gamma)De_Z - De_A, \quad (A5)$$

$$S_D = -De_D + De_P + \gamma De_Z + (1-\beta_P)G_P - \beta_D G_D \quad (A6)$$

The terms in these equations are given in Table A1.

Note that unlike the model of (Popova et al., 2006) we use a continuous model, with no change of equations (bar one exception) above or below the photic zone. For our purposes, the photic zone is defined as 100 m water depth. First we calculate θ:

$$\theta = \frac{\mathrm{Chl}}{\mathrm{P}\zeta} \quad (A7)$$

However, at low light levels, Chl might be zero, therefore we take the limit that $\theta \rightarrow \zeta$ at low levels ($1e^{-7}$) of chlorophyll or phytoplankton.

We then calculate α:

$$\alpha = \alpha_c \theta \quad (A8)$$

OSD
10, 1997–2051, 2013

using the PAR available at each vertex of the mesh the light-limited phytoplankton growth rate, J, is then calculated:

$$J = \frac{v\alpha I_n}{\sqrt{v^2 + \alpha^2 + I_n^2}} \tag{A9}$$

This can be used to calculate the limiting factors on nitrate and ammonium:

$$Q_N = \frac{N\exp^{-\Psi A}}{K_N + N}, \tag{A10}$$

$$Q_A = \frac{A}{K_A + A} \tag{A11}$$

From these the diagnostic field, primary production (X_P), can be calculated:

$$X_P = J(Q_N + Q_A)P \tag{A12}$$

The chlorophyll growth scaling factor is given by:

$$R_P = Q_N Q_A \left(\frac{\theta_m}{\theta}\right)\left(\frac{v}{\sqrt{v^2 + \alpha^2 + I_n^2}}\right) \tag{A13}$$

The zooplankton grazing terms are now calculated:

$$G_P = \frac{gp_P P^2 Z}{\epsilon + \left(p_P P^2 + p_D D^2\right)}, \tag{A14}$$

$$G_D = \frac{gp_D D^2 \cdot Z}{\epsilon + \left(p_P P^2 + p_D D^2\right)} \tag{A15}$$

OSD
10, 1997–2051, 2013

Finally, the four death rates and re-mineralisation rates are calculated:

$$\mathrm{De_P} = \frac{\mu_\mathrm{P} P^2}{P + k_\mathrm{P}} + \lambda_\mathrm{bio} \cdot P, \tag{A16}$$

$$\mathrm{De_Z} = \frac{\mu_\mathrm{Z} Z^3}{Z + k_\mathrm{Z}} + \lambda_\mathrm{bio} \cdot Z, \tag{A17}$$

$$\mathrm{De_D} = \mu_\mathrm{D} D + \lambda_\mathrm{bio} \cdot P + \lambda_\mathrm{bio} \cdot Z, \tag{A18}$$

$$\mathrm{De_A} = \lambda_\mathrm{A} A \quad \text{where } z < 100 \tag{A19}$$

A2 Photosynthetically active radiation (PAR)

The photosynthetically active radiation, or PAR is calculated by:

$$\mathrm{PAR} = (A_\mathrm{water} + A_\mathrm{P} P) I, \tag{A20}$$

where A_water and A_P are the absorption rates of photosynthetically active radiation by water and phytoplankton respectively.

A3 Detritus falling velocity

Detritus is assumed to be denser than water and so sinks slowly through the water column. This is modelled by modifying the advecting velocity in the advection-diffusion equation for detritus by subtracting a sinking velocity u_sink from the vertical component of the advecting velocity.

Acknowledgements. All authors were funded by NERC under Grants NE/F00270X/1 and NE/F004184/1. The authors would like to acknowledge the use of the Imperial College London HPC service to perform some of the simulations presented here.

OSD
10, 1997–2051, 2013

References

Anderson, T. R. and Pondaven, P.: Non-redfield carbon and nitrogen cycling in the Sargasso Sea: pelagic imbalances and export flux, Deep-Sea Res. Pt. I, 50, 573–591, doi:10.1016/S0967-0637(03)00034-7, 2003. 2000, 2009

Burchard, H. and Beckers, J.-M.: Non-uniform adaptive vertical grids in one-dimensional numerical ocean models, Ocean Model., 6, 51–81, doi:10.1016/S1463-5003(02)00060-4, 2004. 2007

Burchard, H. and Bolding, K.: Comparative analysis of four second-moment turbulence closure models for the oceanic mixed layer, J. Phys. Oceanogr., 31, 1943–1968, doi:10.1175/1520-0485(2001)031<1943:CAOFSM>2.0.CO;2, 2001. 2000, 2009

Denman, K. and Miyake, M.: Upper layer modification at Ocean Station Papa: observations and simulation, J. Phys. Oceanogr., 3, 185–196, 1973. 2000, 2009

Farrell, P., Piggott, M., Pain, C., Gorman, G., and Wilson, C.: Conservative interpolation between unstructured meshes via supermesh construction, Comput. Method. Appl. M., 198, 2632–2642, doi:10.1016/j.cma.2009.03.004, 2009. 2007, 2014

Ford, R., Pain, C. C., Piggott, M. D., Goddard, A. J. H., de Oliveira, C. R. E., and Umpleby, A. P.: A nonhydrostatic finite-element model for three-dimensional stratified oceanic flows, Part 1: Model formulation, Mon. Weather Rev., 132, 2816–2831, doi:10.1175/MWR2824.1, 2004. 2001

Gaspar, P., Grégoris, Y., Lefevre, J.-M., and Goris, Y. G. R. I.: A simple eddy kinetic energy model for simulations of the oceanic vertical mixing: tests at station Papa and long-term upper ocean study site, J. Geophys. Res., 95, 16179–16193, doi:10.1029/JC095iC09p16179, 1990. 2000

Hanert, E., Deleersnijder, E., and Legat, V.: An adaptive finite element water column model using the Mellor-Yamada level 2.5 turbulence closure scheme, Ocean Model., 12, 205–223, doi:10.1016/j.ocemod.2005.05.003, 2006. 2007

Hiester, H., Piggott, M., and Allison, P.: The impact of mesh adaptivity on the gravity current front speed in a two-dimensional lock-exchange, Ocean Model., 38, 1–21, doi:10.1016/j.ocemod.2011.01.003, 2011. 2000, 2007, 2013

Hill, J., Piggott, M., Ham, D., Popova, E., and Srokosz, M.: On the performance of a generic length scale turbulence model within an adaptive finite element ocean model, Ocean Model.,

OSD
10, 1997–2051, 2013

56, 1–15, doi:10.1016/j.ocemod.2012.07.003, 2012. 2000, 2002, 2003, 2006, 2009, 2011, 2014, 2015, 2017
Hofmeister, R., Burchard, H., and Beckers, J.-M.: Non-uniform adaptive vertical grids for 3-D numerical ocean models, Ocean Model., 33, 70–86, doi:10.1016/j.ocemod.2009.12.003, 2010. 2007
Kleypas, J. A. and Doney, S. C.: Nutrients, Chlorophyll, Primary Production and related Biogeochemical Properties in the Ocean Mixed Layer, Tech. Rep. TN-447+STR, NCAR, available at: http://dss.ucar.edu/datasets/ds259.0/, 2001. 2009
Large, W. G. and Yeager, S. G.: Diurnal to decadal global forcing for ocean and sea-ice models: the data sets and flux climatologies, Tech. Rep. Technical Report TN-460+STR, NCAR, 2004. 2002
Lévy, M., Iovino, D., Resplandy, L., Klein, P., Madec, G., Tréguier, A.-M., Masson, S., and Takahashi, K.: Large-scale impacts of submesoscale dynamics on phytoplankton: local and remote effects, Ocean Model., 43–44, 77–93, doi:10.1016/j.ocemod.2011.12.003, 2012. 1999
Loseille, A. and Alauzet, F.: Continuous mesh framework, Part 2: Validations and applications, SIAM J. Numer. Anal., 49, 61–86, doi:10.1137/10078654X, 2011. 2007
Madec, G.: NEMO ocean engine, Tech. rep., 2008. 2005
McGillicuddy, D. J., Anderson, L. A., Doney, S. C., and Maltrud, M. E.: Eddy-driven sources and sinks of nutrients in the upper ocean: results from a 0.1° resolution model of the North Atlantic, Global Biogeochem. Cy., 17, 1035, doi:10.1029/2002GB001987, 2003. 1999
Oschlies, A.: Can eddies make ocean deserts bloom?, Global Biogeochem. Cy., 16, 1106, doi:10.1029/2001GB001830, 2002. 1999
Pain, C. C., Umpleby, A. P., de Oliveira, C. R. E., and Goddard, A. J. H.: Tetrahedral mesh optimisation and adaptivity for steady-state and transient finite element calculations, Comput. Method. Appl. M., 190, 3771–3796, doi:10.1016/S0045-7825(00)00294-2, 2001. 2006, 2007
Pain, C. C., Piggott, M., Goddard, A., Fang, F., Gorman, G., Marshall, D., Eaton, M., Power, P., and de Oliveira, C.: Three-dimensional unstructured mesh ocean modelling, Ocean Model., 10, 5–33, doi:10.1016/j.ocemod.2004.07.005, 2005. 2001
Piggott, M. D., Pain, C. C., Gorman, G. J., Power, P. W., and Goddard, A. J. H.: h, r, and hr adaptivity with applications in numerical ocean modelling, Ocean Model., 10, 95–113, doi:10.1016/j.ocemod.2004.07.007, 2005. 2006, 2007
Piggott, M. D., Gorman, G. J., Pain, C. C., Allison, P. A., Candy, A. S., Martin, B. T., and Wells, M. R.: A new computational framework for multi-scale ocean modelling

OSD
10, 1997–2051, 2013

based on adapting unstructured meshes, Int. J. Numer. Meth. Fl., 56, 1003–1015, doi:10.1002/fld.1663, 2008. 2001, 2002, 2006, 2007

Piggott, M. D., Farrell, P. E., Wilson, C. R., Gorman, G. J., and Pain, C. C.: Anisotropic mesh adaptivity for multi-scale ocean modelling, Philos. T. Roy. Soc. A, 367, 4591–4611, doi:10.1098/rsta.2009.0155, 2009. 2002

Popova, E. E., Coward, A. C., Nurser, G. A., de Cuevas, B., Fasham, M. J. R., and Anderson, T. R.: Mechanisms controlling primary and new production in a global ecosystem model – Part I: Validation of the biological simulation, Ocean Sci., 2, 249–266, doi:10.5194/os-2-249-2006, 2006. 2003, 2009, 2019, 2020

Umlauf, L. and Burchard, H.: A generic length-scale equation for geophysical turbulence models, J. Mar. Res., 61, 235–265, doi:10.1357/002224003322005087, 2003. 2003, 2004

Uppala, S. M., Kållberg, P. W., Simmons, A. J., Andrae, U., Bechtold, V. D. C., Fiorino, M., Gibson, J. K., Haseler, J., Hernandez, A., Kelly, G. A., Li, X., Onogi, K., Saarinen, S., Sokka, N., Allan, R. P., Andersson, E., Arpe, K., Balmaseda, M. A., Beljaars, A. C. M., Berg, L. V. D., Bidlot, J., Bormann, N., Caires, S., Chevallier, F., Dethof, A., Dragosavac, M., Fisher, M., Fuentes, M., Hagemann, S., Hólm, E., Hoskins, B. J., Isaksen, L., Janssen, P. A. E. M., Jenne, R., Mcnally, A. P., Mahfouf, J.-F., Morcrette, J.-J., Rayner, N. A., Saunders, R. W., Simon, P., Sterl, A., Trenberth, K. E., Untch, A., Vasiljevic, D., Viterbo, P., and Woollen, J.: The ERA-40 re-analysis, Q. J. Roy. Meteor. Soc., 131, 2961–3012, doi:10.1256/qj.04.176, 2005. 2002

Weber, L., Völker, C., Oschlies, A., and Burchard, H.: Iron profiles and speciation of the upper water column at the Bermuda Atlantic Time-series Study site: a model based sensitivity study, Biogeosciences, 4, 689–706, doi:10.5194/bg-4-689-2007, 2007. 2000

OSD
10, 1997–2051, 2013

Table 1. Weighting of fields used for each metric used in this study. A – indicates this field was not used in the metric construction. See Eq. (19).

Metric	Nutrient (ε)	PAR (ε)	Velocity (ε)	Density (ε)
Bio	10.0	0.1	–	–
Phys	–	–	(0.1, 0.1, 10.0)	0.01
Bio and Phys	10.0	–	(0.1, 0.1, 10.0)	0.01
PAR	–	0.1	–	–

OSD
10, 1997–2051, 2013

Table 2. RMS error, ϵ, of fixed mesh simulations compared to the simulation with 2.5 m vertical resolution at Station Papa. ϵ is shown for mixed layer depth (MLD), and the $L2_{norm}$ of nutrient, primary productivity, chlorophyll, and zooplankton. See Fig. 6 also.

Res (m)	ϵ_{MLD}	ϵ_N	ϵ_P	ϵ_C	ϵ_Z	No. elements
5 m	5.244	0.119	0.098	0.0095	0.0045	1200
10 m	10.640	0.506	0.342	0.0445	0.0169	600
20 m	16.521	0.421	0.628	0.0486	0.0283	300

OSD
10, 1997–2051, 2013

Table 3. RMS error, ϵ, of fixed mesh simulations compared to the simulation with 2.5 m vertical resolution at Bermuda. ϵ is shown for mixed layer depth (MLD), and the $L2_{norm}$ of nutrient, primary productivity, chlorophyll, and zooplankton. See Fig. 7 also.

Res (m)	ϵ_{MLD}	ϵ_N	ϵ_P	ϵ_C	ϵ_Z	No. elements
5 m	7.079	0.408	0.140	0.0129	0.0113	1200
10 m	12.630	0.402	0.149	0.0160	0.0236	600
20 m	18.710	0.397	0.226	0.0285	0.0410	300

OSD
10, 1997–2051, 2013

Table 4. RMS error, ϵ, of fixed mesh simulations compared to the simulation with 2.5 m vertical resolution at Station India. ϵ is shown for mixed layer depth (MLD), and the $L2_{norm}$ of nutrient, primary productivity, chlorophyll, and zooplankton. See Fig. 8 also.

Res (m)	ϵ_{MLD}	ϵ_N	ϵ_P	ϵ_C	ϵ_Z	No. elements
5 m	137.03	1.04	303.258	1.538	0.222	2400
10 m	138.18	1.21	357.834	1.770	0.247	1200
20 m	142.71	1.50	455.565	1.992	0.264	600

OSD
10, 1997–2051, 2013

Table 5. RMS error, ϵ, of adaptive mesh simulations compared to the simulation with 2.5 m vertical resolution at Station Papa. ϵ is shown for mixed layer depth (MLD), and the $L2_{norm}$ of nutrient, primary productivity, chlorophyll, and zooplankton. See Fig. 6 also.

Res (m)	ϵ_{MLD}	ϵ_N	ϵ_P	ϵ_C	ϵ_Z	No. elements (Mean, min, max)
5 m	5.244	0.119	0.0986	0.0095	0.0045	1200
Bio and Phys	4.769	0.053	0.385	0.0038	0.0020	458.5, 372, 558
Bio Only	14.211	0.589	0.529	0.0426	0.0300	386.1, 336, 450
Phys Only	4.837	0.070	0.398	0.0034	0.0021	310.1, 240, 408
PAR	23.324	2.664	0.592	0.0790	0.0330	612.2, 532, 660

OSD
10, 1997–2051, 2013

Table 6. RMS error, ϵ, of adaptive mesh simulations compared to the simulation with 2.5 m vertical resolution at Bermuda. ϵ is shown for mixed layer depth (MLD), and the $L2_{norm}$ of nutrient, primary productivity, chlorophyll, and zooplankton. Note that the PAR and Bio only simulations failed and recorded no result. See Fig. 7 also.

Res (m)	ϵ_{MLD}	ϵ_N	ϵ_P	ϵ_C	ϵ_Z	No. elements
5 m	7.079	0.408	0.140	0.0129	0.0113	1200
Bio and Phys	7.309	0.407	0.598	0.0084	0.0096	310.3, 264, 444
Phys Only	8.432	0.408	0.615	0.0076	0.0082	228.3, 174, 436

OSD
10, 1997–2051, 2013

Table 7. RMS error, ϵ, of adaptive mesh simulations compared to the simulation with 2.5 m vertical resolution at Station India. ϵ is shown for mixed layer depth (MLD), and the $L2_{norm}$ of nutrient, primary productivity, chlorophyll, and zooplankton. See Fig. 8 also.

Res (m)	ϵ_{MLD}	ϵ_N	ϵ_P	ϵ_C	ϵ_Z	No. elements
5 m	137.03	1.04	303.258	1.538	0.222	2400
Bio and Phys	141.98	1.12	356.798	1.668	0.236	287.74, 150.0, 456.0
Bio Only	112.72	1.12	324.777	1.052	0.097	220.63, 120.0, 360.0
Phys Only	141.30	1.08	344.102	1.683	0.237	249.53, 150.0, 414.0
PAR	131.84	1.17	677.312	1.920	0.245	120.00, 120.0, 121.0

OSD
10, 1997–2051, 2013

Table A1. Symbols used to describe the six-component NPZD model. Typical values are provided for externally set parameters.

Symbol	Meaning	Typical value	Equation
α	initial slope of $P-I$ curve in $\mathrm{Wm^{-2}\,day^{-1}}$		(A8)
α_c	Chl *a* specific initial slope of $P-I$ curve	$2\,\mathrm{g\,C\,(g\,Chl)^{-1}\,Wm^{-2}\,day^{-1}}$	
β_P, β_D	assimilation coefficients of zooplankton	0.75	
De_D	rate of breakdown of detritus to ammonium		(A18)
De_P	rate of phytoplankton natural mortality		(A16)
De_Z	rate of zooplankton natural mortality		(A17)
De_A	ammonium nitrification rate		(A19)
δ	excretion parameter	0.7	
ϵ	grazing parameter relating capture of prey items to prey density	0.4	
G_P	rate of zooplankton grazing on phytoplankton		(A14)
G_D	rate of zooplankton grazing on detritus		(A15)
g	zooplankton maximum growth rate	$1.3\,\mathrm{day^{-1}}$	
γ	fraction of zooplankton mortality going to detritus	0.5	
I_0	photosynthetically active radiation (PAR) immediately below surface of water. Assumed to be 0.43 of the surface radiation		
J	light-limited phytoplankton growth rate in $\mathrm{day^{-1}}$		(A9)
k_A	half-saturation constant for ammonium uptake	$0.5\,\mathrm{mmol\,m^{-3}}$	
k_N	half-saturation constant for nitrate uptake	$0.5\,\mathrm{mmol\,m^{-3}}$	
k_P	half-saturation constant for phytoplankton mortality	$1\,\mathrm{mmol\,m^{-3}}$	
k_Z	half-saturation constant for zooplankton mortality	$3\,\mathrm{mmol\,m^{-3}}$	
k_w	light attenuation due to water	$0.04\,\mathrm{m^{-1}}$	
k_c	light attenuation due to phytoplankton	$0.03\,\mathrm{m^2\,mmol^{-1}}$	
λ_{bio}	rate of the phytoplankton and zooplankton transfer into detritus	$0.05\,\mathrm{day^{-1}}$	
λ_A	nitrification rate	$0.03\,\mathrm{day^{-1}}$	
μ_P	phytoplankton mortality rate	$0.05\,\mathrm{day^{-1}}$	
μ_Z	zooplankton mortality rate	$0.2\,\mathrm{day^{-1}}$	
μ_D	detritus reference mineralisation rate	$0.05\,\mathrm{day^{-1}}$	
Ψ	strength of ammonium inhibition of nitrate uptake	$2.9\,\mathrm{mmol\,m^{-3}})^{-1}$	
p_P	relative grazing preference for phytoplankton	0.75	
p_D	relative grazing preference for detritus	0.25	
Q_N	non-dimensional nitrate limiting factor		(A10)
Q_A	non-dimensional ammonium limiting factor		(A11)
R_P	Chl growth scaling factor		(A13)
v	Maximum phytoplankton growth rate	$1\,\mathrm{day^{-1}}$	
w_g	detritus sinking velocity	$10\,\mathrm{m\,day^{-1}}$	
z	depth		
θ	Chl to carbon ratio in $\mathrm{mg\,Chl\,(mg\,C)^{-1}}$		
θ_m	maximum Chl to carbon ratio	$0.05\,\mathrm{mg\,Chl\,(mg\,C)^{-1}}$	
ζ	conversion factor from g C to mmol N based on C : N ratio of 6.5	$0.0128\,\mathrm{mmol\,N\,(ng\,C)^{-1}}$	

OSD
10, 1997–2051, 2013

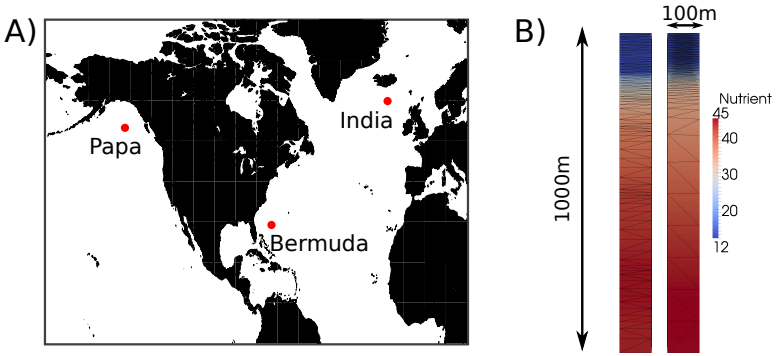

Fig. 1. Map of station locations **(A)** and two-dimensional view of the model domain at showing two different meshes produced by the adaptivity algorithm **(B)**.

OSD
10, 1997–2051, 2013

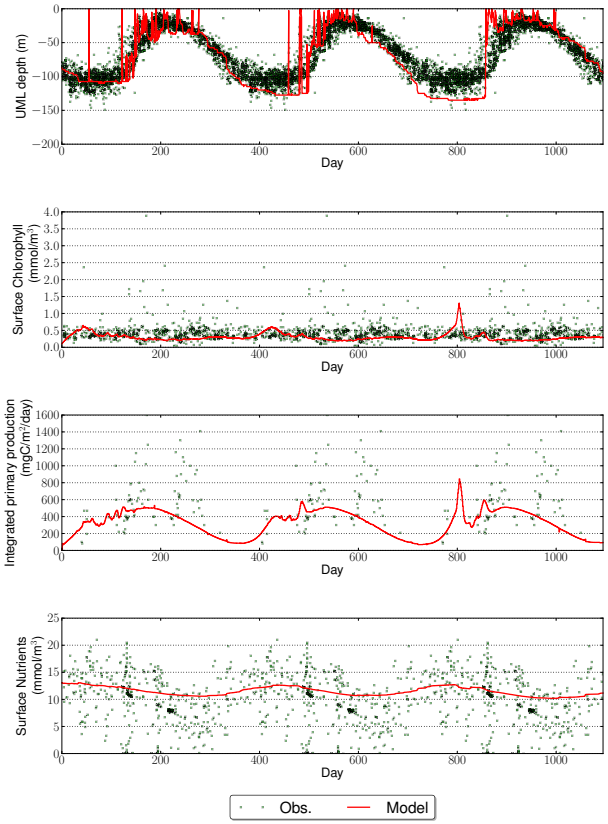

Fig. 2. Summary of simulated physical and biological behaviour at Station Papa for a uniform (2.5 m), non-adaptive simulation. From top to bottom panels show MLD, surface chlorophyll, integrated primary productivity and surface nutrients. Where available, measured data are show as green squares. Measured data are plotted against year day due to lack of data for some quantities.

OSD
10, 1997–2051, 2013




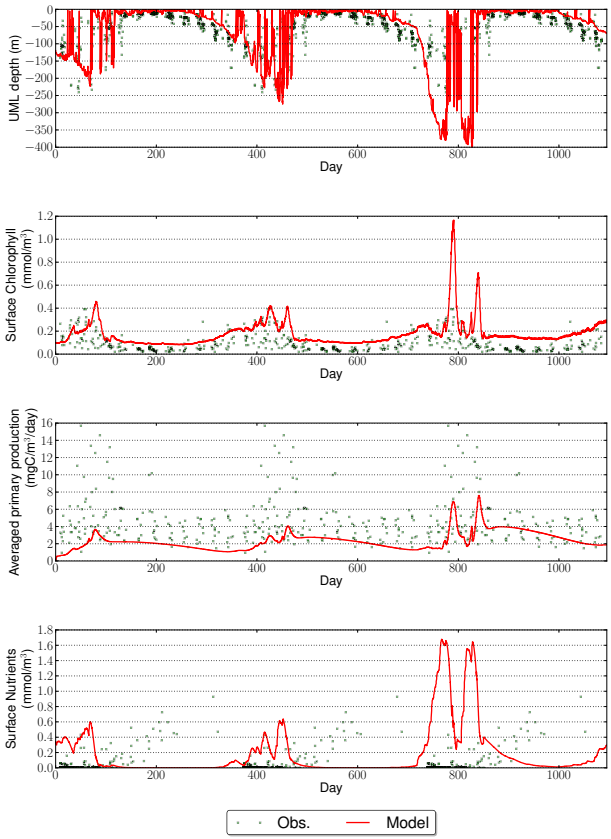

Fig. 3. Summary of simulated physical and biological behaviour at Bermuda for a uniform (2.5 m), non-adaptive simulation. From top to bottom panels show MLD, surface chlorophyll, averaged primary productivity and surface nutrients. Where available, measured data are show as green squares. Measured data are plotted against year day due to lack of data for some quantities.

OSD
10, 1997–2051, 2013




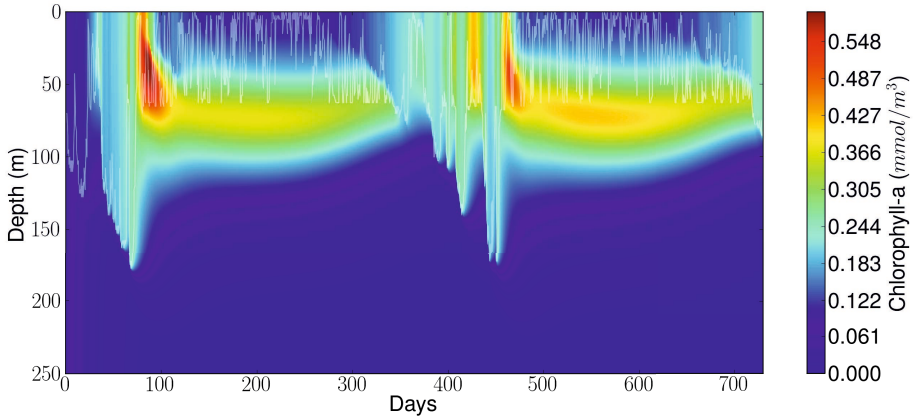

Fig. 4. Time-depth plot of chlorophyll at Bermuda, showing the clear subsurface chlorophyll maxima.

OSD
10, 1997–2051, 2013

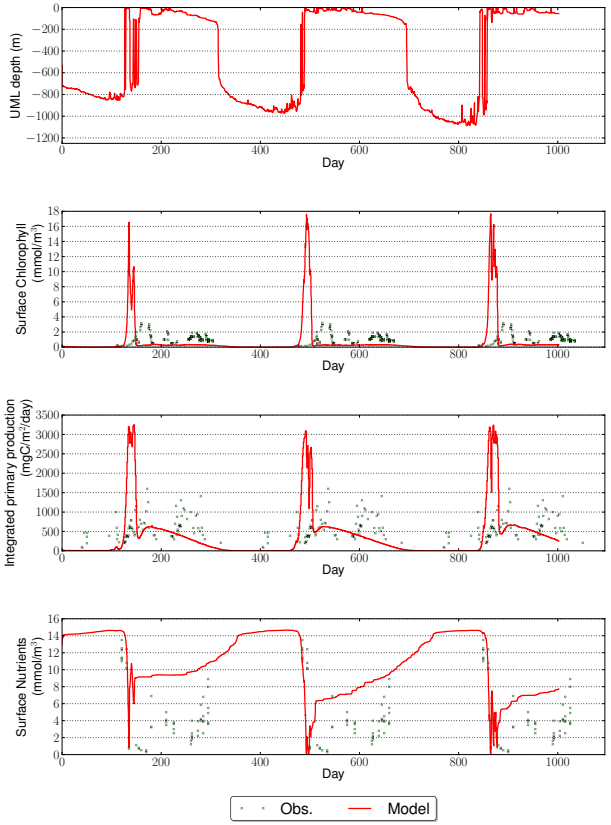

Fig. 5. Summary of simulated physical and biological behaviour at Station India for a uniform (2.5 m), non-adaptive simulation. From top to bottom panels show MLD, surface chlorophyll, integrated primary productivity and surface nutrients. Where available, measured data are show as green squares. Measured data are plotted against year day due to lack of data for some quantities.

OSD
10, 1997–2051, 2013

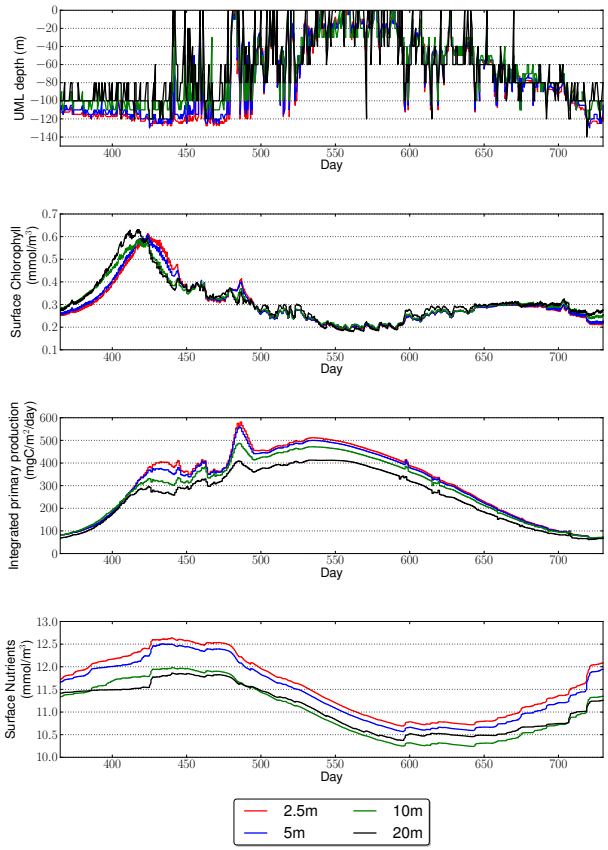

Fig. 6. Summary of simulated physical and biological behaviour at Station Papa using uniform meshes at a number of resolutions. From top to bottom panels show MLD, surface chlorophyll, integrated primary productivity and surface nutrients.

OSD
10, 1997–2051, 2013

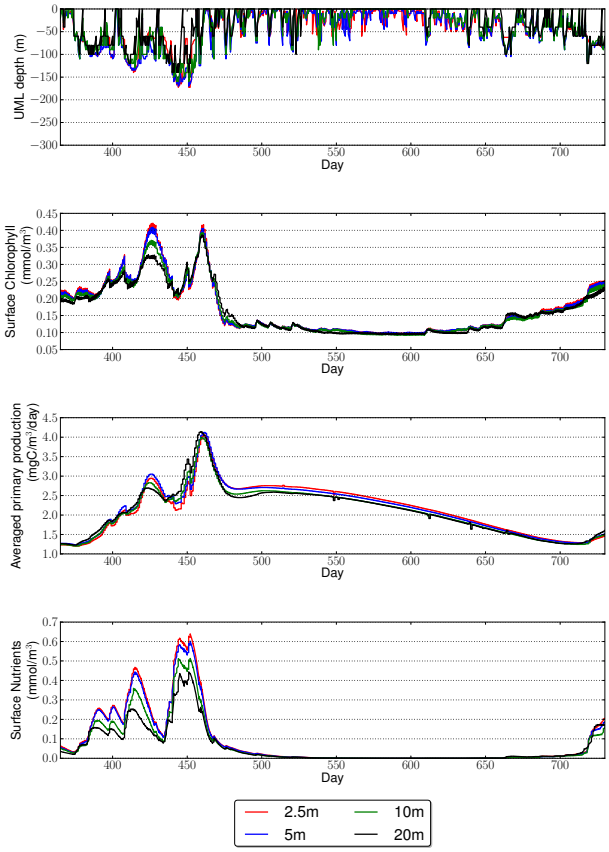

Fig. 7. Summary of simulated physical and biological behaviour at Bermuda using uniform meshes at a number of resolutions. From top to bottom panels show MLD, surface chlorophyll, MLD averaged primary productivity and surface nutrients.

OSD
10, 1997–2051, 2013

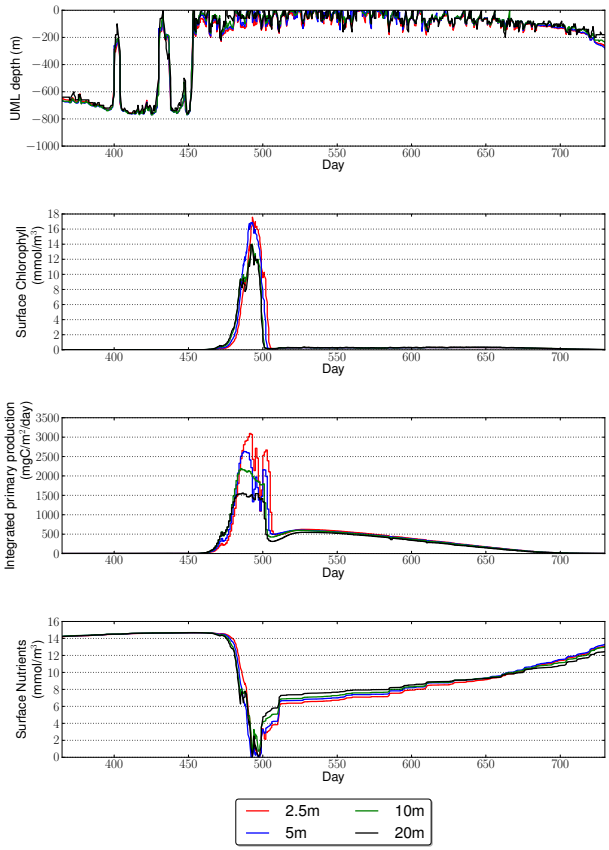

Fig. 8. Summary of simulated physical and biological behaviour at Station India using uniform meshes at a number of resolutions. From top to bottom panels show MLD, surface chlorophyll, integrated primary productivity and surface nutrients.

OSD
10, 1997–2051, 2013

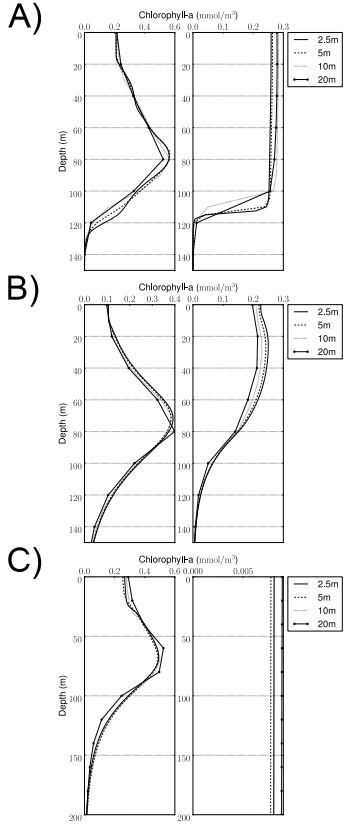

Fig. 9. Vertical profiles of chlorophyll at **(A)** Station Papa, **(B)** Bermuda and **(C)** Station India over the top 150 m, 150 m and 200 m respectively using uniform meshes at a number of resolutions. The left-hand column shows the profile in summer (day 182) and the right- hand side shows the column in winter (day 365). There are changes in values at key depths of upto 15 % depending on the vertical resolution used.

OSD
10, 1997–2051, 2013

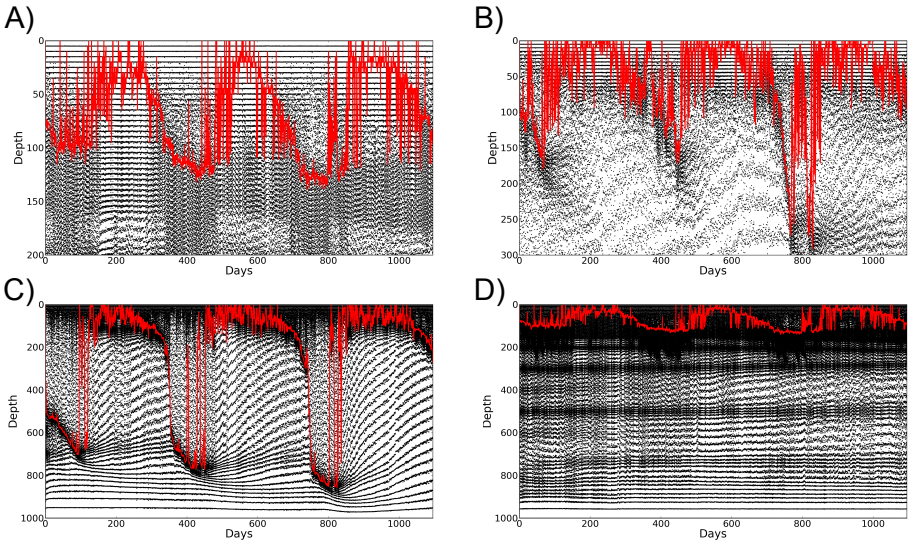

Fig. 10. Representation of the meshes obtained via adaptivity for all stations using the *bio and phys* metric. A dot is placed on each vertex in the mesh and this is repeated for each output time. Clustering of vertices therefore indicate higher resolution. Station Papa **(A)** shows reduced resolution under the mixed layer during summer, but high resolution persists for some distance below the mixed layer. Bermuda **(B)** shows substantial reduction of resolution below the mixed layer, but with the minimum resolution being maintained during the summer in the upper layers. Similarly, India **(C)** tracks the mixed layer depth, with decreased resolution within the MLD, whilst maintaining good resolution in the upper portion of the water column. Gradients in density mean that high resolution zones are maintained at Station Papa **(D)** at depths of upto 800 m depth.

OSD
10, 1997–2051, 2013

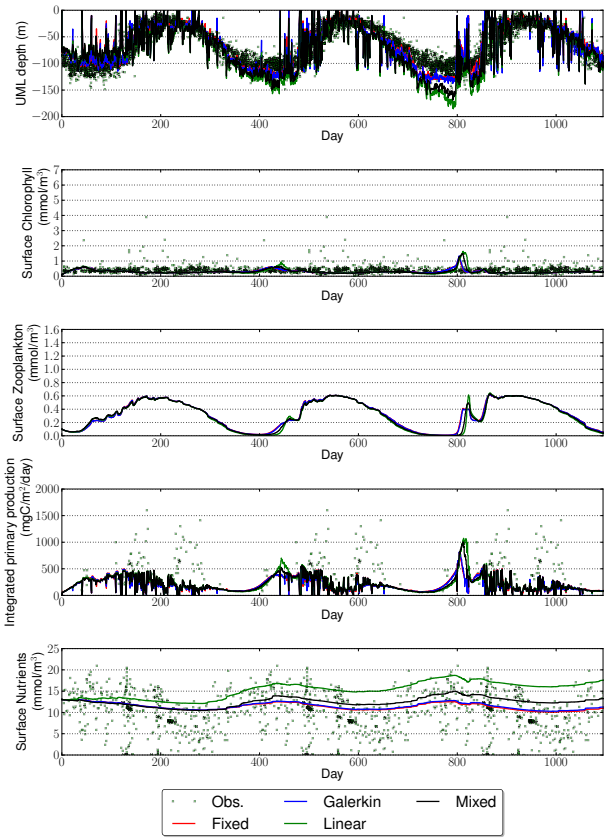

Fig. 11. Summary of simulation results from Station Papa comparing the fixed high resolution (2.5 m) simulation with adaptive simulation using different interpolation methods between meshes. Linear and mixed perform poorly, inducing extra vertical diffusivity, compared to Galerkin projection. Panels and data are the same as in Fig. 6.

OSD
10, 1997–2051, 2013

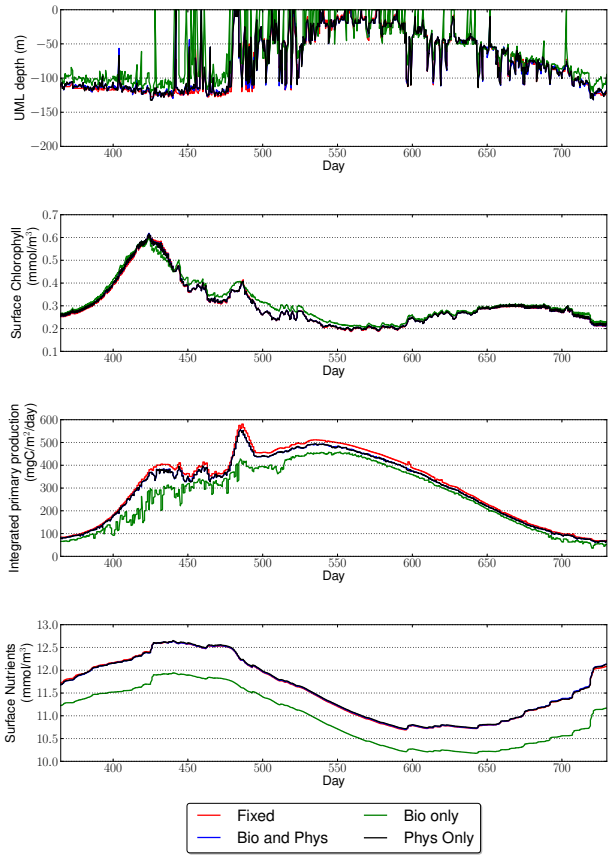

Fig. 12. Summary of results comparing different adaptivity metrics against measured data and the high resolution (2.5 m) fixed mesh simulation for Station Papa.

OSD
10, 1997–2051, 2013




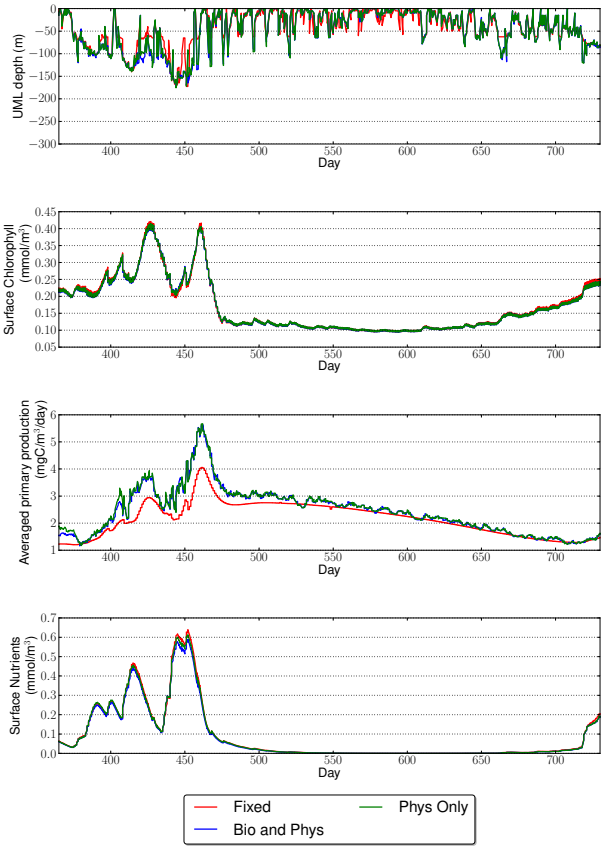

Fig. 13. Summary of results comparing different adaptivity metrics against measured data and the high resolution (2.5 m) fixed mesh simulation at Bermuda. Note the simulations using PAR and biology only failed after only a few adapts.

OSD
10, 1997–2051, 2013

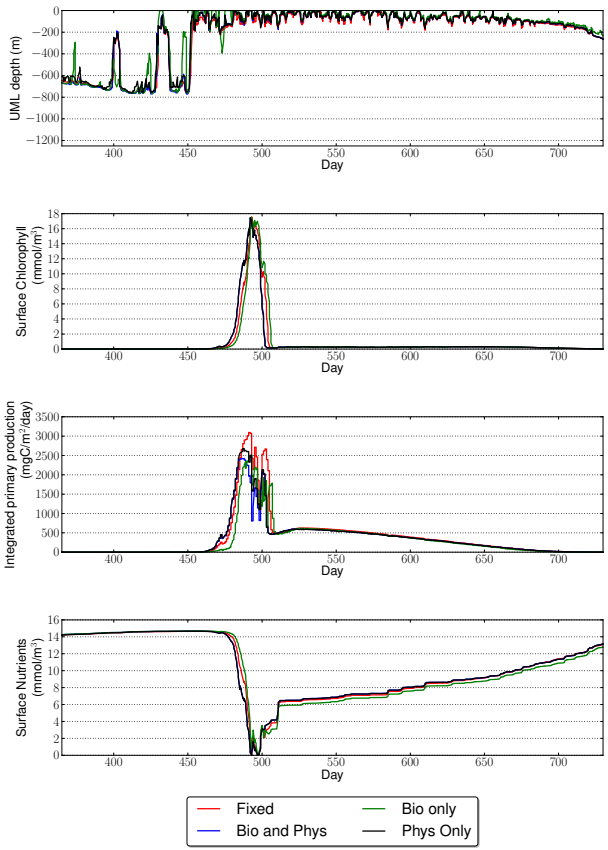

Fig. 14. Summary of results comparing different adaptivity metrics against measured data and the high resolution (2.5 m) fixed mesh simulation for Station India.

OSD
10, 1997–2051, 2013

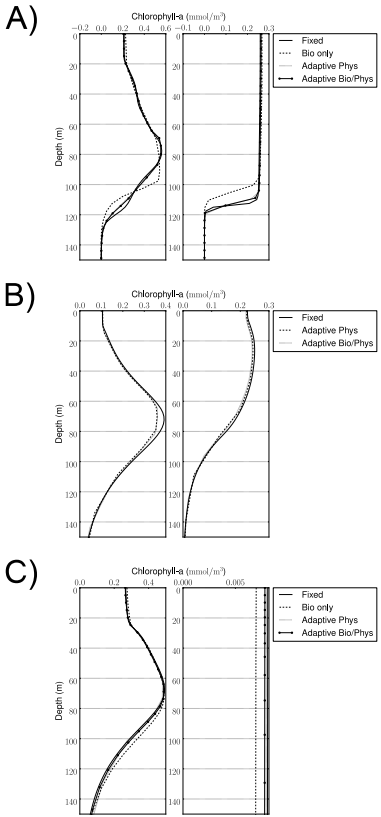

Fig. 15. Vertical profiles of chlorophyll at **(A)** Station Papa, **(B)** Bermuda and **(C)** Station India over the top 150 m, 150 m and 200 m respectively comparing the performance of different adaptivity metrics. The left-hand column shows the profile in summer (day 182) and the right-hand side shows the column in winter (day 365). Note that all metrics, bar biology only show similar results.

OSD
10, 1997–2051, 2013

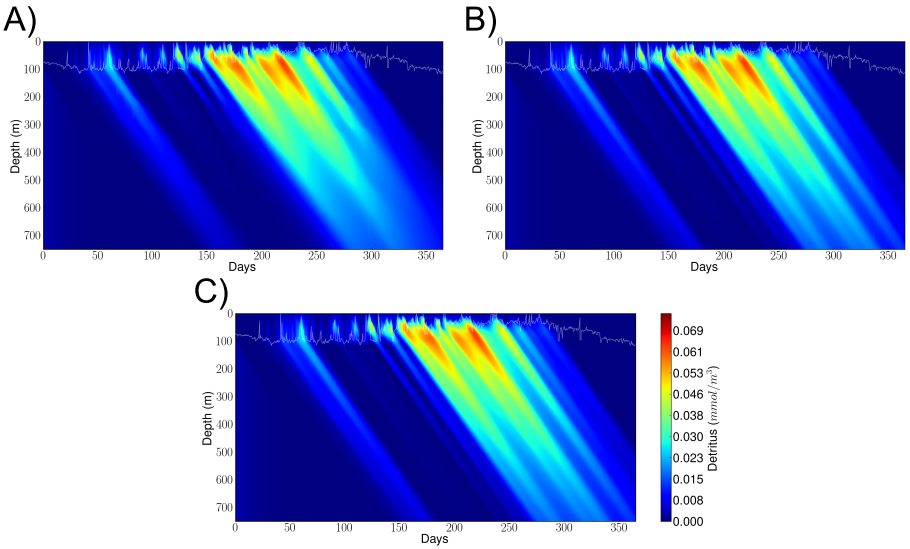

Fig. 16. Time-depth plot of detritus at station papa from the original adaptive mesh simulation **(A)**, the adaptive run with detritus included in the metric **(B)** and the high resolution fixed mesh simulation **(C)**.

OSD
10, 1997–2051, 2013

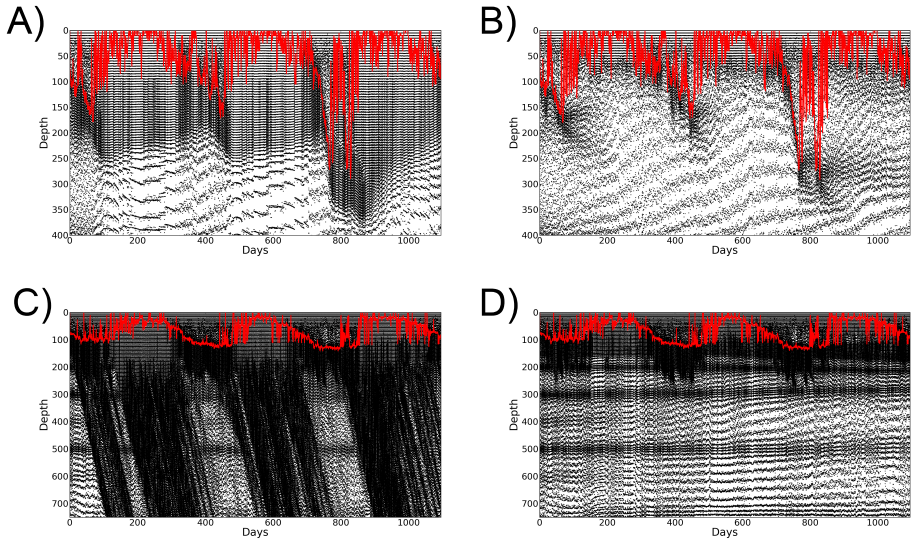

Fig. 17. Comparison of meshes produced by adaptive simulations. **(A)** Bermuda with the addition of chlorophyll to the adaptivity metric, **(B)** the original adaptive simulation at Bermuda using velocity, density and nutrients. Similarly, for Station Papa; **(C)** adaptive simulation with detritus included in the metric and **(D)** original adaptive simulation.

OSD
10, 1997–2051, 2013

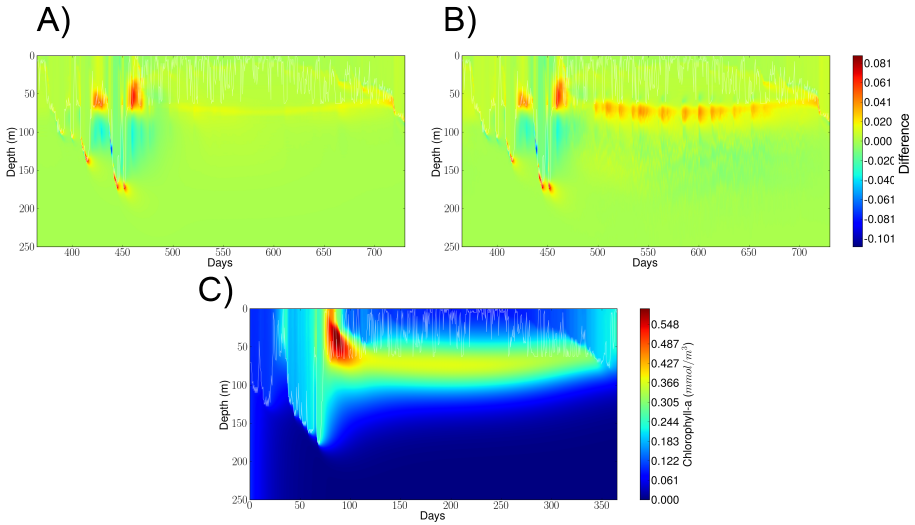

Fig. 18. Difference plots of chlorophyll at Bermuda comparing adaptive simulations (**A** and **B**) to the high resolution (2.5 m) uniform mesh simulation. A clear improvement can be made in the subsurface chlorophyll maximum representation by adding chlorophyll to the adaptivity metric. **(A)** the adaptive run with chlorophyll included in the metric, **(B)** the original adaptive mesh simulation, and **(C)** the high resolution uniform mesh simulation showing the values of chlorophyll.

OSD
10, 1997–2051, 2013